



Thermal analyses of LiFePO₄/graphite battery discharge processes

Fangming Jiang*, Peng Peng, Yiqiong Sun

Laboratory of Advanced Energy Systems, CAS Key Laboratory of Renewable Energy, Guangzhou Institute of Energy Conversion, Chinese Academy of Sciences (CAS), Guangzhou 510640, China



HIGHLIGHTS

- We develop an electrochemical–thermal model for LiFePO₄/graphite batteries.
- Various heat sources/sinks are fully handled in this model.
- Model results provide detailed insight into the battery discharge processes.
- Comprehensive thermal analyses to discharge processes are conducted.
- Distribution and evolution of heat sources/sinks are extensively scrutinized.

ARTICLE INFO

Article history:

Received 5 February 2013

Received in revised form

2 May 2013

Accepted 20 May 2013

Available online 28 May 2013

Keywords:

Thermal analyses

Lithium iron phosphate battery

Electrochemical–thermal model

Discharge process

ABSTRACT

An electrochemical–thermal coupling model is developed to describe the LiFePO₄/graphite battery discharge and charge processes. Various heat generations/consumptions including Joule heat, reversible entropy heat, contact resistance heat, irreversible electrochemical reaction heat, ionic migration heat, and convective heat release to the ambient during charge or discharge processes are calculated in detail. The developed model is first validated by experimental data. Then systematic and comprehensive thermal analyses with respect to various discharge processes are performed based on the simulated results. For the specific cell considered, the irreversible electrochemical reaction heat and contact resistance heat are found to be the two main heat generation sources; for discharge processes of higher C-rate, the contact resistance heat take more proportion of the total heat generation as it is directly proportional to the squared discharge current density; the ionic migration heat is a sink with magnitude being about 1/3 of the Joule heat. The reversible entropy heat changes its sign from a negative heat sink to a positive heat source during a discharge process and its changing magnitude may be comparable to the irreversible electrochemical reaction heat for all the discharge processes of different C-rates.

© 2013 Published by Elsevier B.V.

1. Introduction

Ever since reported by Padhi et al. [1] in 1997, the LiFePO₄ has been considered to be one of the most promising positive electrode materials for lithium-ion batteries. Although the gravimetric and volumetric energy density of LiFePO₄ cathode is lower than other cathode materials that are based on rare metal composites (LiCoO₂, LiNiO₂ etc.), the LiFePO₄ is a favorable choice as cathode material for lithium-ion batteries in electric vehicle (EV) and medium- to large-sized energy storage applications due to its stable and safe olivine structure as well as lower cost and environment-benign essence. However, the practical utilization of LiFePO₄/graphite batteries continuously reminds us that the safety issue is still a major

challenge for this type of battery. Improper design and abusive operations are identified to be the major reasons causing safety accidents. A robust and powerful mathematical–physical model that addresses the complex mechanism of relevant processes and can be used as an effective tool for thermal analyses, structural design, and thermal management design of LiFePO₄/graphite batteries is thus critically needed.

Numerical modeling is widely used and plays an important role in the research of electrochemical and thermal performance of lithium-ion battery. Various electrochemical–thermal (ECT) coupling models for lithium-ion batteries were developed and extensively discussed in public literature [2–5]. These models are based on the electrochemical (EC) model proposed by Doyle et al. [6,7] in combination of an energy conservation equation with various heat generations/consumptions formulated. During battery operations, the heat generations/consumptions contain the Joule

* Corresponding author. Tel.: +86 20 87057656.

E-mail addresses: fm_jiang2000@yahoo.com, fm_jiang2013@yahoo.com (F. Jiang).

Nomenclature	
A	side surface area of the electrode plate (m^2)
a_s	specific surface area (m^{-1})
c	Li^+ concentration (mol m^{-3})
c_p	specific heat capacity ($\text{J kg}^{-1} \text{K}^{-1}$)
D	diffusion coefficient ($\text{m}^2 \text{s}^{-1}$)
F	Faraday's constant (C mol^{-1})
h	convective heat transfer coefficient ($\text{W m}^{-2} \text{K}^{-1}$)
I	current load (A)
i_0	exchange current density (A m^{-2})
j_{Li}	transfer current density (A m^{-3})
L	through-plane thickness of the battery (m)
L_e	through-plane thickness of the electrode (m)
p	Bruggeman factor
q	volumetric heat generation rate (W m^{-3})
Q	heat generation rate (W)
r	radius of solid active particles (m)
R_{c1}	contact resistance at the electrode and current collector interface ($\Omega \text{ m}^2$)
R_{c2}	contact resistance at the electrolyte and solid phase interface ($\Omega \text{ m}^2$)
R_c	the total lumped contact resistance ($\Omega \text{ m}^2$)
R	universal gas constant ($\text{J mol}^{-1} \text{K}^{-1}$)
T	temperature (K)
T_{amb}	ambient temperature (K)
T_{ref}	reference temperature (K)
T_{surface}	temperature at the cell surface (K)
t	time (s)
t_+^0	transference number of Li^+ dissolved in the electrolyte
U	open-circuit potential (V)
V	cell voltage (V)
<i>Greek symbols</i>	
α_a	anodic transfer coefficient
α_c	cathodic transfer coefficient
ϵ	porosity
η	surface overpotential (V)
κ	ionic conductivity (S m^{-1})
λ	thermal conductivity ($\text{W m}^{-1} \text{K}^{-1}$)
ρ	density (kg m^{-3})
σ	electronic conductivity (S m^{-1})
φ	electric potential (V)
<i>Subscripts/superscripts</i>	
e	electrolyte phase
s	solid phase
neg	negative electrode
pos	positive electrode
sep	separator

heat (ionic + electronic ohmic heat), ionic migration heat, irreversible EC reaction heat, reversible entropy heat, electric contact resistance heat at the current collector/electrode interface and that caused by the SEI layer covering the solid phase, and heat release to the ambient. All of these heats vary with time and space. Analyzing the spatial distribution and temporal evolution of these heats is very important to the design, operation and thermal management of batteries.

Srinivasan et al. [8], Zhang [9], and Ye et al. [10] analyzed the thermal behavior of LiMn_2O_4 battery. However they did not consider the heat generation due to electric contact resistance and a comprehensive thermal analysis was generally not conducted. For LiFePO_4 /graphite batteries, the differences of physicochemical property such as, the temperature characteristics of open circuit potential that dictate heat generations, between LiFePO_4 and other cathode materials may lead to completely different thermal behaviors. Thermal analyses of LiFePO_4 /graphite battery discharge/charge processes have been seldom reported to date. In the present work we perform a comprehensive and systematical thermal analysis with respect to various discharge processes (1C, 3C and 5C) of a LiFePO_4 /graphite battery based on the simulated results from a self-developed ECT coupling model. The ECT model solves the inter-coupled charge (ion in the electrolyte and electron in the solid phase), species (Li^+ in the electrolyte and lithium in electrode active materials) and energy conservation equations. Modeling results are validated by experimental data first. Then various heat generations/consumptions including the Joule heat, reversible entropy heat, contact resistance heat, irreversible EC reaction heat, ionic migration heat, and convective heat release to the ambient during discharge processes are calculated and analyzed in detail.

2. Model

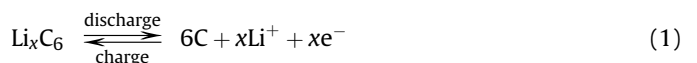
The developed model is 3-dimensional, consisting of an electrochemical model and a thermal model, termed as ECT coupling model.

2.1. Electrochemical model

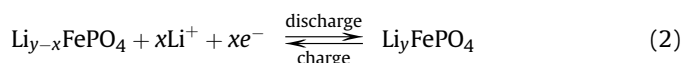
Fig. 1 schematically shows the physical model of a LiFePO_4 /graphite battery considered in the present ECT model. The cell consists of a copper current collector, a negative electrode, a separator, a positive electrode and an aluminum current collector. Both the electrodes and the separator are all porous. The electrode is composed of active material, electrolyte, polymer binder and conductive filler. The active materials of anode and cathode are commonly graphite mesocarbon microbeads and LiFePO_4 (LFP), respectively. The electrolyte is commonly lithium hexa-fluorophosphate (LiPF_6) in a mixture of propylene carbonate, ethylene carbonate and dimethyl carbonate. The porous separator is composed of liquid electrolyte and polymer matrix. Illustrated also in Fig. 1 is the assumed Li transport model in solid particles of anode and cathode active materials.

During charge/discharge processes, the electrochemical reactions occurring in electrodes can be expressed as follows.

in the anode composite electrode,



in the cathode composite electrode,



The electrochemical model for LiFePO_4 /graphite battery developed in this work is based on porous electrode and concentrated solution theories [6,7]. Major assumptions are described as the following.

(1) Electrode active materials are considered to be spherical particles of uniform size.

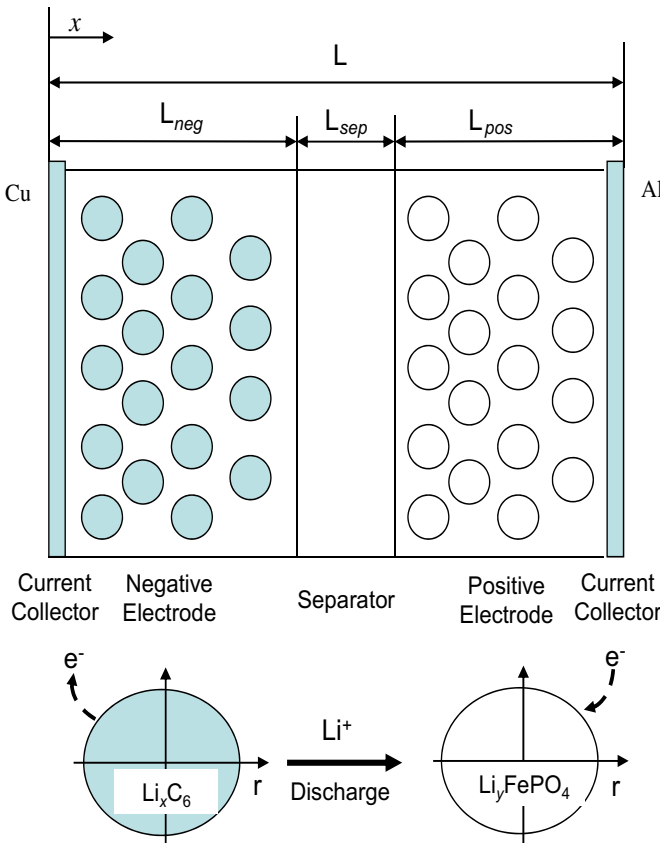


Fig. 1. Physical model of a LiFePO₄/graphite battery.

- (2) Side reactions are ignored and no gas phase is present during charge/discharge processes.
- (3) The electrolyte is considered to be concentrated binary solution, namely, it is dissociated into a cation and an anion [11].
- (4) Li⁺ transport in the electrolyte relies on diffusion and migration and in the solid active material particles diffusion only.
- (5) Electrochemical reaction rates of Li⁺ insertion and extraction processes are assumed to follow the Butler–Volmer equation, which describes a large class of electrode reactions.
- (6) Interfacial electrical and chemical equilibrium exist at the electrode/electrolyte interface.

To account for tortuosity effects, the ionic conductivity and diffusion coefficient in the electrolyte phase are corrected in terms of the Bruggeman theorem, $\kappa_{\text{eff}} = \kappa_e^{\text{P}}$ and $D_e = D_e \epsilon_e^{\text{P}}$. Likewise, for each electrode the electronic conductivity is corrected as $\sigma_{\text{eff}} = \sigma \epsilon_s^{\text{P}}$. Here, ϵ_s and ϵ_e are the volume fractions of solid and electrolyte phase, respectively.

In numerical modeling, we treat the battery as a single-domain of multiple sub-regions associated with different sets of characteristic properties. This circumvents difficulties about matching boundary conditions at the interior interfaces of the battery. Following is presented the mathematical model in detail.

2.1.1. Charge conservation in solid phase

The charge conservation equation for electron transport in the solid phase can be described as follows:

$$\frac{\partial}{\partial x} \left(\sigma_{\text{eff}} \frac{\partial \varphi_s}{\partial x} \right) + \frac{\partial}{\partial y} \left(\sigma_{\text{eff}} \frac{\partial \varphi_s}{\partial y} \right) + \frac{\partial}{\partial z} \left(\sigma_{\text{eff}} \frac{\partial \varphi_s}{\partial z} \right) - j^{\text{Li}} = 0 \quad (3)$$

with boundary conditions:

$$-\sigma - \frac{\partial \varphi_s}{\partial x} \Big|_{x=0} = -\sigma + \frac{\partial \varphi_s}{\partial x} \Big|_{x=L} = \frac{I}{A} \quad (4)$$

Constant current density related to the discharge/charge current load is imposed at the outer surface of the current collector for both anode and cathode side. All the other boundaries are with zero flux boundary condition. As the boundary conditions expressed by Eq. (4) are both flux type, and the flux values are equal to each other, a deterministic solution to Eq. (3) needs a φ_s reference point. In the present work, a φ_s reference point (-3.02 V) is set in the anode current collector.

2.1.2. Charge conservation in electrolyte phase

The charge conservation equation for ion transport in the electrolyte phase can be expressed as follows:

$$\begin{aligned} \frac{\partial}{\partial x} \left(\kappa_{\text{eff}} \frac{\partial \varphi_e}{\partial x} \right) + \frac{\partial}{\partial y} \left(\kappa_{\text{eff}} \frac{\partial \varphi_e}{\partial y} \right) + \frac{\partial}{\partial z} \left(\kappa_{\text{eff}} \frac{\partial \varphi_e}{\partial z} \right) + \frac{\partial}{\partial x} \left(\kappa_D^{\text{eff}} \frac{\partial \ln c_e}{\partial x} \right) \\ + \frac{\partial}{\partial y} \left(\kappa_D^{\text{eff}} \frac{\partial \ln c_e}{\partial y} \right) + \frac{\partial}{\partial z} \left(\kappa_D^{\text{eff}} \frac{\partial \ln c_e}{\partial z} \right) + j^{\text{Li}} = 0 \end{aligned} \quad (5)$$

with boundary conditions:

$$\frac{\partial \varphi_e}{\partial x} \Big|_{x=0} = \frac{\partial \varphi_e}{\partial x} \Big|_{x=L} = 0 \quad (6)$$

All the other boundaries are with zero flux boundary condition also. There is no ionic charge flux in the anode and cathode current collectors.

The electrolyte considered is lithium hexafluorophosphate (LiPF₆) in a mixture of 10 vol% propylene carbonate, 27 vol% ethylene carbonate and 63 vol% dimethyl carbonate. The ionic conductivity is taken from the experimental data of our industrial partner, Amperex Technology Limited (ATL).

$$\begin{aligned} \kappa = 20.8409c_e - 21.29c_e^2 + 13.6986c_e^3 - 7.58544c_e^4 \\ + 2.45464c_e^5 - 0.30446c_e^6 \end{aligned} \quad (7)$$

Fig. 2 plots the fitting curve of the ionic conductivity as a function of Li⁺ concentration.

The diffusional conductivity, κ_D^{eff} is determined by virtue of concentrated solution theory, as

$$\kappa_D^{\text{eff}} = \frac{2R\kappa^{\text{eff}}}{F} \left(t_+^0 - 1 \right) \left(1 + \frac{d\ln f_{\pm}}{d\ln c_e} \right) \quad (8)$$

where f_{\pm} is the mean molar activity coefficient of the electrolyte.

2.1.3. Species conservation in solid phase

In LiFePO₄ electrode the solid active particles generally undergo a phase change with lithiated and unlithiated forms having distinct phases, known as two-phase coexistence during charge/discharge processes. The shrinking-core model initially proposed by Padhi et al. [1] was commonly used to model lithium species transport in solid LiFePO₄ particles [12–16], whereas experimental evidence by Laffont et al. [17] and Chen et al. [18] indicated that a shrinking-core model might not be an accurate representation of the phase-change process. One other model presented by Andersson et al. [19] namely mosaic model can probably better explain the mechanism for lithium extraction/insertion within a given particle in LiFePO₄ electrode, but there is lack of a good mathematical description to the mosaic model to date due to the complexity. Though there may exist other alternatives to the shrinking-core

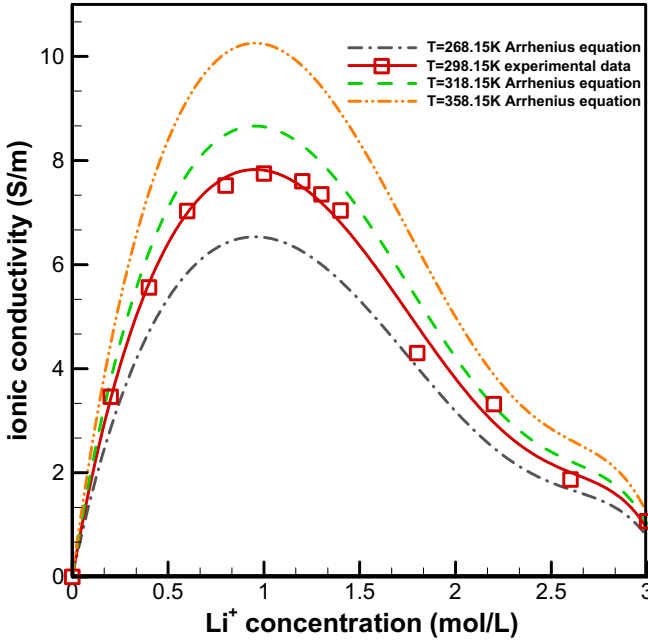


Fig. 2. Ionic conductivity as a function of Li^+ concentration and temperature.

model, such as a phase-field model based on Cahn–Hilliard theory [20–23] and a so-called resistive-reactant model [24,25], models using Fickian diffusion equation are of practical values due to the low computational cost and ease of implementation for both charge and discharge processes [26,27]. Apparently, the application of Fick's law to Li transport in LiFePO_4 active particles with lithiated and unlithiated two-phases coexisting [27] has assumed that the phase transition behaviors phenomenally follow Fick's law though the motive force of phase transition is essentially not the Li concentration difference. The present modeling effort also takes this assumption and the species conservation equation for lithium transport in anode and cathode active materials can thus be expressed as follows:

$$\frac{\partial c_s}{\partial r} = D_s \left(\frac{\partial^2 c_s}{\partial r^2} + \frac{2}{r} \frac{\partial c_s}{\partial r} \right) \quad (9)$$

with boundary conditions:

$$\left. \frac{\partial c_s}{\partial r} \right|_{r=0} = 0 \quad (10)$$

$$j^{\text{Li}}(t) = -a_s F D_s \left. \frac{\partial c_s}{\partial r} \right|_{r=R} \quad (11)$$

The diffusive flux at the surface of the solid active particle is determined from the electrochemical reaction rate.

A constant diffusion coefficient, $1.25 \times 10^{-15} \text{ m}^2 \text{ s}^{-1}$, which is within the range of Li diffusivity in LiFePO_4 presented in Ref. [28], in the cathode solid phase is taken empirically, while that in the anode is a function of state of charge (SOC) [29], expressed as

$$D_s = 3.9 \times 10^{-14} (1.5 - \text{SOC})^{3.5} \quad (12)$$

2.1.4. Species conservation in electrolyte phase

The species conservation equation for Li^+ species transport in the electrolyte phase is formulated as:

$$\begin{aligned} \frac{\partial (\varepsilon_e c_e)}{\partial t} &= \frac{\partial}{\partial x} \left(D_e^{\text{eff}} \frac{\partial c_e}{\partial x} \right) + \frac{\partial}{\partial y} \left(D_e^{\text{eff}} \frac{\partial c_e}{\partial y} \right) + \frac{\partial}{\partial z} \left(D_e^{\text{eff}} \frac{\partial c_e}{\partial z} \right) \\ &\quad + \frac{1 - t_+^0}{F} j^{\text{Li}} \end{aligned} \quad (13)$$

with boundary conditions:

$$\left. \frac{\partial c_e}{\partial x} \right|_{x=0} = \left. \frac{\partial c_e}{\partial x} \right|_{x=L} = 0 \quad (14)$$

All the other boundaries are with zero flux boundary condition also. In the current collectors there is no Li^+ diffusive flux.

The Li^+ diffusion coefficient in the electrolyte is taken from literature [30], as

$$D_e = 10^{-8.43 - 54.0/(T - 229 - 5c_e) - 0.22c_e} \quad (15)$$

Table 1 summarizes the governing equations and boundary conditions of the electrochemical model.

2.1.5. Electrochemical kinetics

The transfer current density j^{Li} , which quantifies the electrochemical reaction rate, is calculated by the Butler–Volmer equation:

$$j^{\text{Li}} = a_s i_0 \left[\exp \left(\frac{\alpha_a F}{RT} \eta \right) - \exp \left(- \frac{\alpha_c F}{RT} \eta \right) \right] \quad (16)$$

The exchange current density i_0 is calculated by:

$$i_0 = k c_e^{\alpha_a} (c_{s,\text{max}} - c_{s,e})^{\alpha_a} c_{s,e}^{\alpha_c} \quad (17)$$

where, k is the reaction rate, $c_{s,e}$ is the lithium concentration at the electrode/electrolyte interface, and $c_{s,\text{max}}$ is the maximum lithium concentration in the solid phase.

The surface overpotential η is defined as:

$$\eta = \varphi_s - \varphi_e - U \quad (18)$$

where the open-circuit potential, U , is a function of $c_{s,e}/c_{s,\text{max}}$ and temperature.

2.2. Thermal model

The thermal model is described by the following energy conservation equation:

$$\begin{aligned} p_c \frac{\partial T}{\partial t} &= \frac{\partial}{\partial x} \left(\lambda^{\text{eff}} \frac{\partial T}{\partial x} \right) + \frac{\partial}{\partial y} \left(\lambda^{\text{eff}} \frac{\partial T}{\partial y} \right) + \frac{\partial}{\partial z} \left(\lambda^{\text{eff}} \frac{\partial T}{\partial z} \right) \\ &\quad + q + \frac{Q_c + Q_v}{dx dy dz} \end{aligned} \quad (19)$$

where q is the summation of all the heat generations/consumptions except the contact resistance heat during the operation of lithium-ion battery and is calculated to be:

$$q = q_r + q_o + q_i + q_e \quad (20)$$

The irreversible electrochemical reaction heat is given by

$$q_r = j^{\text{Li}}(\varphi_s - \varphi_e - U) = j^{\text{Li}}\eta \quad (21)$$

Table 1
Governing equations and boundary conditions of the EC model

	Conservation equations	Boundary conditions
Charge, solid phase	$\frac{\partial}{\partial x} \left(\sigma^{\text{eff}} \frac{\partial \varphi_s}{\partial x} \right) + \frac{\partial}{\partial y} \left(\sigma^{\text{eff}} \frac{\partial \varphi_s}{\partial y} \right) + \frac{\partial}{\partial z} \left(\sigma^{\text{eff}} \frac{\partial \varphi_s}{\partial z} \right) - j^{li} = 0$	$-\sigma_{+} \frac{\partial \varphi_s}{\partial x} \Big _{x=0} = -\sigma_{-} \frac{\partial \varphi_s}{\partial x} \Big _{x=L} = \frac{I}{A}; \text{Zero flux at other boundaries}$
Charge, electrolyte phase	$\frac{\partial}{\partial x} \left(\kappa^{\text{eff}} \frac{\partial \varphi_e}{\partial x} \right) + \frac{\partial}{\partial y} \left(\kappa^{\text{eff}} \frac{\partial \varphi_e}{\partial y} \right) + \frac{\partial}{\partial z} \left(\kappa^{\text{eff}} \frac{\partial \varphi_e}{\partial z} \right) + \frac{\partial}{\partial x} \left(\kappa_D^{\text{eff}} \frac{\partial \ln c_e}{\partial x} \right) + \frac{\partial}{\partial y} \left(\kappa_D^{\text{eff}} \frac{\partial \ln c_e}{\partial y} \right) + \frac{\partial}{\partial z} \left(\kappa_D^{\text{eff}} \frac{\partial \ln c_e}{\partial z} \right) + j^{li} = 0$	$\frac{\partial \varphi_e}{\partial x} \Big _{x=0} = \frac{\partial \varphi_e}{\partial x} \Big _{x=L} = 0; \text{Zero flux at other boundaries}$
Species, solid phase	$\frac{\partial c_s}{\partial t} = D_s \left(\frac{\partial^2 c_s}{\partial x^2} + \frac{2 \partial c_s}{r \frac{\partial r}{\partial x}} \right)$	$\frac{\partial c_s}{\partial r} \Big _{r=0} = 0; j^{li}(t) = -a_s F P_s \frac{\partial c_s}{\partial r} \Big _{r=R}$
Species, electrolyte phase	$\frac{\partial (c_e c_e)}{\partial t} = \frac{\partial}{\partial x} \left(D_e^{\text{eff}} \frac{\partial c_e}{\partial x} \right) + \frac{\partial}{\partial y} \left(D_e^{\text{eff}} \frac{\partial c_e}{\partial y} \right) + \frac{\partial}{\partial z} \left(D_e^{\text{eff}} \frac{\partial c_e}{\partial z} \right) + \frac{1 - r_+^0}{F} j^{li}$	$\frac{\partial c_e}{\partial x} \Big _{x=0} = 0; j^{li}(t) = -a_s F P_s \frac{\partial c_e}{\partial x} \Big _{x=L} = 0; \text{Zero flux at other boundaries}$

The ohmic heat is calculated by

$$q_o = \sigma^{\text{eff}} \left[\left(\frac{\partial \varphi_s}{\partial x} \right)^2 + \left(\frac{\partial \varphi_s}{\partial y} \right)^2 + \left(\frac{\partial \varphi_s}{\partial z} \right)^2 \right] + \kappa^{\text{eff}} \left[\left(\frac{\partial \varphi_e}{\partial x} \right)^2 + \left(\frac{\partial \varphi_e}{\partial y} \right)^2 + \left(\frac{\partial \varphi_e}{\partial z} \right)^2 \right] \quad (22)$$

where the first term on the right hand side (RHS) represents the electronic ohmic heat and the second term ionic ohmic heat. The ionic migration heat is given by

$$q_i = \kappa_D^{\text{eff}} \left(\frac{\partial \ln c_e}{\partial x} \frac{\partial \varphi_e}{\partial x} + \frac{\partial \ln c_e}{\partial y} \frac{\partial \varphi_e}{\partial y} + \frac{\partial \ln c_e}{\partial z} \frac{\partial \varphi_e}{\partial z} \right) \quad (23)$$

The reversible entropic heat is given by

$$q_e = j^{\text{Li}} T \frac{\partial U}{\partial T} \quad (24)$$

The contact resistance heat is calculated by

$$Q_c = I^2 \frac{R_{c1}}{A} + \iiint (j^{\text{Li}})^2 \frac{1}{a_s} R_{c2} dx dy dz \quad (25)$$

where the first term on the RHS represents the heat generation due to the contact resistance at the interface of electrode and current collector, the second term the heat generation due to the contact resistance at the interface of electrolyte and solid actives (SEI). In the present modeling effort, we lump the effects of electric contact resistance between the current collector and electrode, R_{c1} , and the impedance due to the SEI layers, R_{c2} , by simply specifying a total contact resistance R_c based on the side surface area of the electrode plate, A .

$$R_c = R_{c1} + \frac{A}{I^2} \iiint (j^{\text{Li}})^2 \frac{1}{a_s} R_{c2} dx dy dz \approx R_{c1} + \frac{1}{L_e a_s} R_{c2} \quad (26)$$

For the derivation of the last term in Eq. (26), we have assumed approximately uniform transfer current density in the electrodes. Hence, we get

$$Q_c = I^2 \frac{R_c}{A} \quad (27)$$

The convective heat dissipation is considered as a heat sink term of numerical elements adjoining the heat release boundaries. It has been included in the source term in Eq. (20), and is given by

$$Q_v = h A (T_{\text{amb}} - T_{\text{surface}}) \quad (28)$$

Therefore, all the outer surfaces of the battery are thermally adiabatic.

2.3. Additional modeling parameters

The open circuit potential (OCP), U , is a function of local state of charge (SOC) or depth of discharge (DOD), and temperature. In the present model, OCP of negative electrode is taken from the experimental data of ATL and OCP of positive electrode from Ref. [12]. Fit curves for anode and cathode OCPs, U_n and U_p as function of SOC or DOD (temperature fixed at 25 °C) are depicted in Fig. 3.

Temperature-change rates of U_n and U_p at different SOC are obtained from Refs. [31,32], respectively. The fit curves are displayed in Fig. 4.

Temperature-dependence for other physicochemical properties can be generally described by the Arrhenius equation,

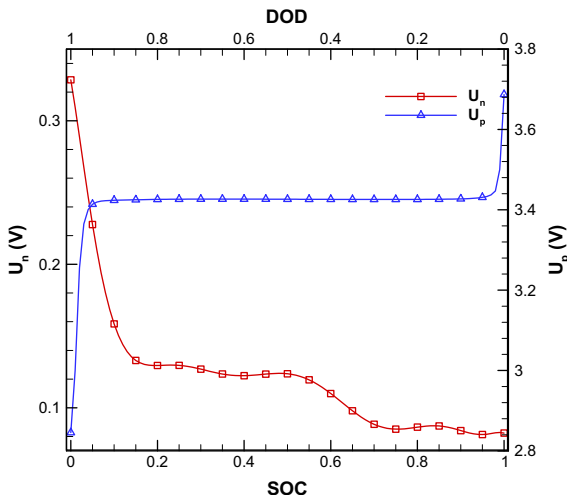


Fig. 3. Open circuit potential of negative electrode (Li_xC_6) U_n and positive electrode (Li_yFePO_4) U_p .

$$\Theta = \Theta_{\text{ref}} \exp \left[\frac{E_{\text{act},\Theta}}{R} \left(\frac{1}{T_{\text{ref}}} - \frac{1}{T} \right) \right] \quad (29)$$

where Θ represents a general parameter, which can be the species diffusivity, ionic conductivity, exchange current density in electrode, etc., with $E_{\text{act},\Theta}$ denoting the corresponding activation energy.

Fig. 2 exemplifies the Arrhenius temperature-dependence of ionic conductivity. It is worth pointing out that the assumption of Arrhenius temperature-dependence of ionic conductivity may be only applicable for normal temperature range (not deviating 298 K too much) and normal solute concentration range (not deviating 1 mol L⁻¹ too much) as the solute dissociation is limited when the solution is highly concentrated, particularly at a low temperature.

Table 2 tabulates the values or calculation equations of some important parameters used in the present modeling and simulations.

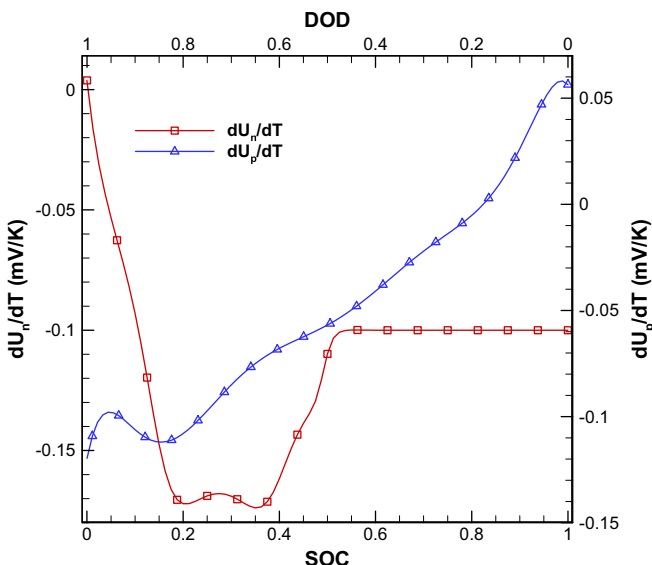


Fig. 4. Entropy change of negative electrode dU_n/dT and positive electrode dU_p/dT as a function of state of charge.

2.4. Numerical strategy

Once appropriate boundary conditions, as exemplified by Eqs. (4), (6), (10), (11), (14), and initial conditions are established, the equation group consisting of Eqs. (3), (5), (9), (13) and (19) is solved for the five unknowns: ϕ_s , ϕ_e , c_e , $c_{s,e}$ ($c_{s,e} = c_s|_{r=R_s}$) and T in the commercial computational fluid dynamics (CFD) flow solver, Fluent®, which is based on the finite volume approximation. By customizing its User Defined Functions (UDF), various source terms and physicochemical properties are implemented. The first order upwind differencing scheme is generally used to discretize the spatial-derivative terms and a fully implicit scheme is used to discretize the transient terms. To accelerate convergence, the algebraic multi-grid (AMG) iterative method is applied to solve the linearized algebraic equations.

3. Experimental validation

We only performed 1D simulations with respect to discharge processes of various C-rates: 1C, 3C and 5C. The geometrical dimensions, including the particle size of solid active materials of the battery and some important model parameters have already been included in Table 2. Individual component volume fraction of the composite electrodes are 67.5% active material, 30.0% electrolyte, and 2.5% additives in the anode; 54.4% active material, 28.0% electrolyte, and 17.65% additives in the cathode; 40.0% electrolyte and 60.0% polymer matrix in the separator. The battery capacity is calculated to be 2.14 mAh cm⁻²; the anode to cathode capacity ratio is 1.05:1. The 1C, 3C and 5C discharge rates are calculated to correspond to 2.14 mA cm⁻² (i.e., 155 mA g⁻¹), 6.42 mA cm⁻² (i.e., 465 mA g⁻¹), and 10.7 mA cm⁻² (i.e., 775 mA g⁻¹) discharge processes, respectively. Initially, the cell temperature is 25 °C; lithium concentration in the anode and cathode active materials are 25,533 mol m⁻³ and 1257 mol m⁻³, respectively; Li⁺ concentration in the electrolyte phase is 1000 mol m⁻³ everywhere. For model validation, we compare the model-predicted cell voltage and temperature with the experimental data. The model-predicted cell voltage is calculated by

$$V = \varphi_s|_{x=L} - \varphi_s|_{x=0} - \frac{R_c}{A} I \quad (30)$$

Fig. 5 compares the simulated and experimental cell voltage during the discharge processes. Overall, the simulated data agree well with the experimental data, especially for the lower C-rate discharge process. There is some discrepancy between the simulated results and experimental data during the very early and late period of the discharge processes, more evident for the two higher C-rate processes. One possible reason is that the interfacial electrical and chemical equilibrium assumption may be violated or to some extent lose validity when the discharge processes are in the last or very early period, particularly for higher C-rate discharge processes.

Fig. 6 compares the simulated battery surface temperature with the experimental data. To account for the effect of thermal natural convection as a function of temperature difference and the effect of heat radiation, the heat convection coefficient used in this study is constant all-through each discharge process, but with different values for discharge processes of different C-rate. For a discharge process we optimized the heat convection coefficient to get best match between experimental and simulated temperature value when SOC approximately equals 0.5. Overall, the simulated temperature curves capture the major characteristics such as varying tendency of the experimental data although only 1D process is assumed. Both the simulated and experimental results show the

Table 2
Model parameters in different regions.

Parameters	Cu current collector	Anode	Separator	Cathode	Al current collector
Thickness ^a L (μm)	9	59	20	92	16
Density [33], ρ (kg m^{-3})	8900	2660	492	1500	2700
Specific heat capacity [33], c_p ($\text{J kg}^{-1} \text{K}^{-1}$)	385	1437.4	1978	1260.2	903
Thermal conductivity [33], λ ($\text{W m}^{-1} \text{K}^{-1}$)	398	1.04	0.334	1.48	238
Particle radius ^a r (μm)		14.75	N/A	1.15	
Porosity ^a e		0.3	0.4	0.28	
Specific area in electrode ^a a_s ($\text{m}^2 \text{m}^{-3}$)		1.065E5		1.366E6	
Maximum Li ⁺ concentration in solid ^a (mol m^{-3})		28688.77	N/A	20950	
Initial SOC ^a		0.8		0.13	
Initial electrolyte concentration ^a c_e (mol m^{-3})		1000	1000	1000	
Reference exchange current density [12] (A m^{-2})		6		2	
Solid phase electronic conductivity, σ (S m^{-1})	6.0E7 [34]	2.0 [29]	0	0.01 [12]	3.8E7 [34]
Ionic conductivity in electrolyte, κ (S m^{-1})	0		Eq. (7) ^a	0	
Li ⁺ diffusion coefficient in electrolyte, D_e ($\text{m}^2 \text{s}^{-1}$)	0		Eq. (15) [30]	0	
Li diffusion coefficient in solid, D_s ($\text{m}^2 \text{s}^{-1}$)			N/A	1.25E-15 [28]	
Activation energy for exchange current density ^a (J mol^{-1})		4000	N/A	4000	
Activation energy for solid phase Li diffusion coefficient ^a (J mol^{-1})		4000	N/A	20000	
Activation energy for ionic conductivity of electrolyte ^a (J mol^{-1})		4000	4000	4000	
Bruggeman exponent [29]		1.5	1.5	1.5	
Anodic/Cathodic transfer coefficient [32], α_a , α_c	0.5			0.5	
Convective heat transfer coefficient, h ($\text{W m}^{-2} \text{K}^{-1}$)			1–1.75		
Transference number [12]			0.363		
contact resistance ^a , R_c (Ωm^2)			0.003		
Faraday's constant, F (C mol^{-1})			96487.0		
Reference temperature ^a (K)			298.15		

^a ATL Data.

temperature rises are ~ 2.5 , 9, and 15°C for 1C, 3C and 5C discharge processes, respectively. Nevertheless there are some discrepancies seen between the simulated and experimental results especially for the two higher C-rate discharge processes. We speculate the major reason may be the assumption of a same constant contact resistance for all the three discharge processes, which disregards the possible temporal dependence of contact resistance at the current collector/electrode interfaces and the spatial and temporal dependence of contact resistance due to SEI. This assumption may bring relatively more significant effects on the temperature evolution during the discharge processes of higher C-rate.

From the above comparisons between the experimental and simulated results, though some discrepancies exist, the reliability and reasonability of the developed ECT coupling model are validated. Following are presented thermal analyses of LiFePO₄/graphite battery discharge processes.

4. Thermal analyses

We simulated 1C, 3C, and 5C discharge processes of the 1D cell. To facilitate analyses and discussion about thermal behaviors of the

discharge processes, we first present the simulated results on spatial and temporal distribution of major variables during 1C discharge process.

Fig. 7 gives the spatial and temporal distribution of the transfer current density, the magnitude of which reflects the EC reaction intensity. Upon loading, EC reactions occur and a transfer current density distribution quickly builds up in both the electrodes. In the anode, the transfer current density is positive, cathode negative. In the anode, we see fluctuations of the transfer current density with time and the location with stronger EC reaction intensity shifts frequently. In the cathode, the transfer current density shows more stable distribution and its maximum magnitude is always seen at locations close to the cathode/separators interface during the early and middle long period of the discharge process. During the late period of the discharge process, the maximum transfer current density location shifts from the cathode/separators interface to the cathode current collector side and in the vicinity regions close to the cathode separator the magnitude of the transfer current density is smaller.

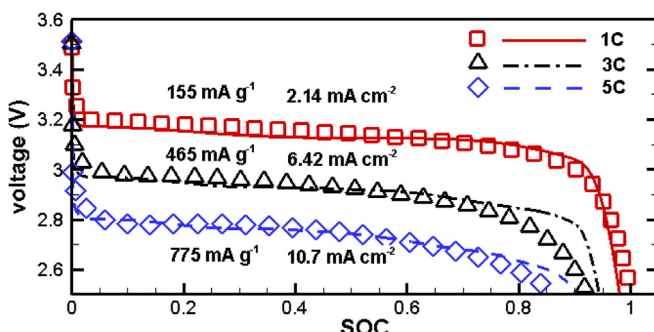


Fig. 5. Comparison of simulated and experimental cell voltage values.

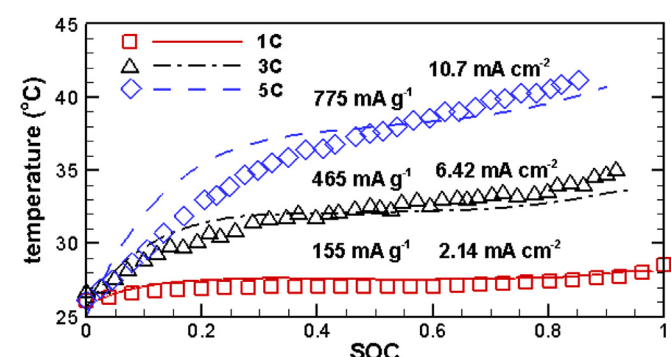


Fig. 6. Comparison of simulated and experimental battery surface temperature values.

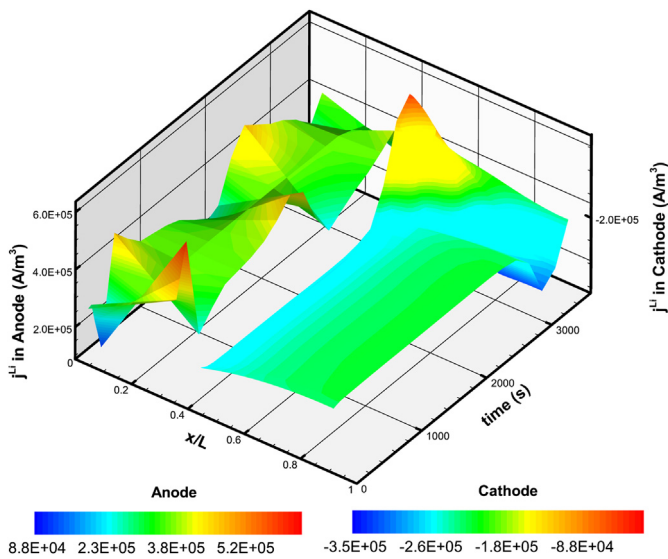


Fig. 7. Spatial and temporal distribution of the transfer current density during 1C discharge process.

The transfer current density relates exponentially with the overpotential by the Butler–Volmer equation, Eq. (16) – overpotential is the driving force of EC reaction. Fig. 8 shows the spatial and temporal distribution of the overpotential. In the anode the overpotential is positive and cathode negative. In the anode, we see the overpotential fluctuating with time and the location of maximum overpotential shifts several times. In the cathode, the overpotential has more stable distribution and its maximum magnitude is always seen at locations close to the cathode/separator interface during the early and middle long period of the discharge process; during the late period of the discharge process, the maximum magnitude of overpotential shifts from the cathode/separator interface to the cathode current collector side. All these accord with the observations from Fig. 7. The overpotential is calculated with Eq. (18), which describes a linear dependence of the overpotential on the solid phase potential (φ_s), electrolyte phase

potential (φ_e), and OCP. To understand the spatial and temporal distribution of the overpotential displayed in Fig. 8, we present the simulated results of φ_s , φ_e , and OCPs in Figs. 9–11, respectively.

Fig. 9 shows the spatial and temporal distribution of the solid phase potential (φ_s). In the cathode, φ_s decreases with time all-through the discharge process as expected due to the increasing DOD; during the very early and late period of the process the OCPs are very sensitive to the DOD (or SOC) and φ_s is thus seen to decrease fast. The absolute value of φ_s in the anode changes little with time as a φ_s reference point (-3.02 V) is set in the anode current collector. In the anode across the cell thickness direction, φ_s slightly decreases with the increase of x and in the cathode it also slightly decreases with the increase of x , forming φ_s gradients to drive electronic charge transport from the separator side to the current collector side in the anode and from the current collector side to the separator side in the cathode.

Fig. 10 gives the spatial and temporal distribution of the electrolyte phase potential (φ_e). It decreases with time all-through the discharge process due to the increasing DOD; during the very late period of the process it changes rapidly because of the high sensitivity of OCPs on DOD (or SOC). Across the cell thickness direction, φ_e decreases with the increase of x , forming a φ_e gradient to drive Li^+ charge transport from the anode to cathode.

Fig. 11 presents the spatial and temporal distribution of the OCPs. Overall, OCP in the anode increases with time while in the cathode decreases. Fast change of the cathode OCP is seen in the very early and late period of the discharge process. Across the cell thickness direction at a same time instant, the anode OCP shows smaller difference while the cathode OCP shows generally larger difference especially during the middle long period of the discharge process, indicating the EC reaction in anode occurs in more uniform mode.

Since $\eta = \varphi_s - \varphi_e - \text{OCP}$ (i.e., Eq. (18)), to explain the spatial and temporal fluctuations of the transfer current density (see Fig. 7) or the overpotential (see Fig. 8) in the anode, we set two monitoring points and compare the temporal evolution of φ_s (and φ_e , OCP, overpotential η) difference between these two points. Results together with the positions of the two monitoring points are depicted in Fig. 12. Seen from this figure, the overpotential at point 1 can be greater or smaller than that at point 2, in accordance to the observations from Fig. 8. Inspection of the variation curves of $(\text{OCP}_2 - \text{OCP}_1)$, $(\varphi_{s2} - \varphi_{s1})$, and $(\varphi_{e2} - \varphi_{e1})$ discovers that the

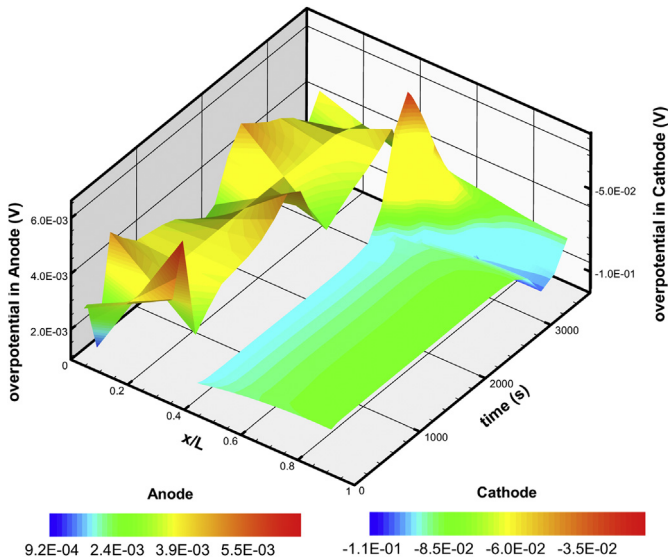


Fig. 8. Spatial and temporal distribution of the overpotential during 1C discharge process.

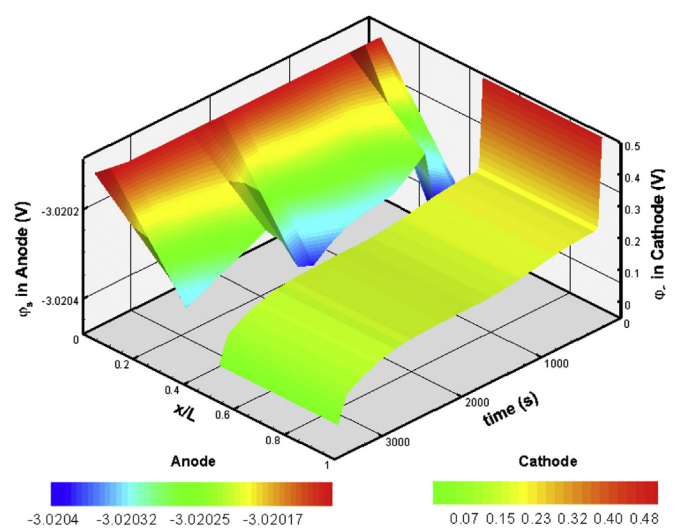


Fig. 9. Spatial and temporal distribution of the solid phase potential during 1C discharge process.

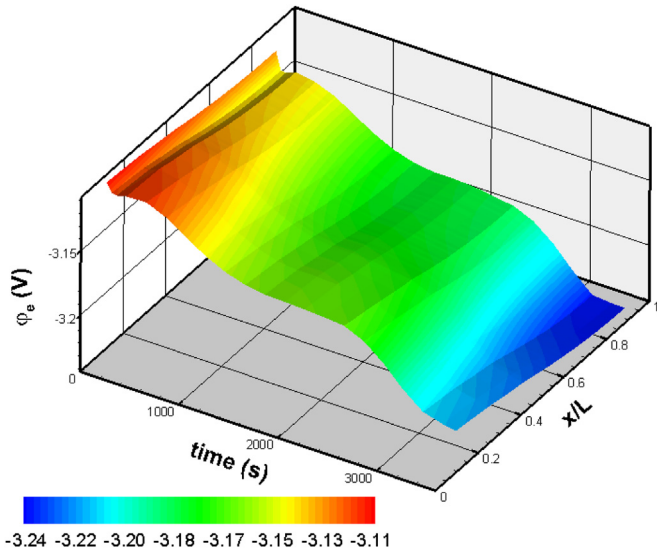


Fig. 10. Spatial and temporal distribution of the electrolyte phase potential during 1C discharge process.

$(\eta_1 - \eta_2)$ curve has a similar variation tendency to $(OCP_2 - OCP_1)$ curve. Therefore we ascertain that the temporal and spatial fluctuations of the overpotential and transfer current density are caused by the fluctuations of OCP. It is seen from Fig. 12 also that the absolute values of $(OCP_2 - OCP_1)$, $(\varphi_{s1} - \varphi_{s2})$, $(\varphi_{e2} - \varphi_{e1})$, and $(\eta_1 - \eta_2)$ are all very small, around couple of millivolts. That is to say, any slight disturbance at the OCP value may cause a fluctuation at the spatial distribution and/or temporal evolution of overpotential η . Checking the OCP–SOC (or DOD) curve for the anode shown in Fig. 3, we deduce that the disturbance at OCP originates from the constitutive OCP–SOC (or DOD) relationship as the OCP–SOC (or DOD) curve is not a perfectly smooth curve, but with quite a few small fluctuations, which may lead to a few millivolt OCP fluctuations even if the SOC (or DOD) values have little difference.

The spatial and temporal distribution of Li concentration at the surface of solid active particles is shown in Fig. 13. The $C_{s,e}/C_{s,max}$ decreases in the anode and increases in the cathode with time as

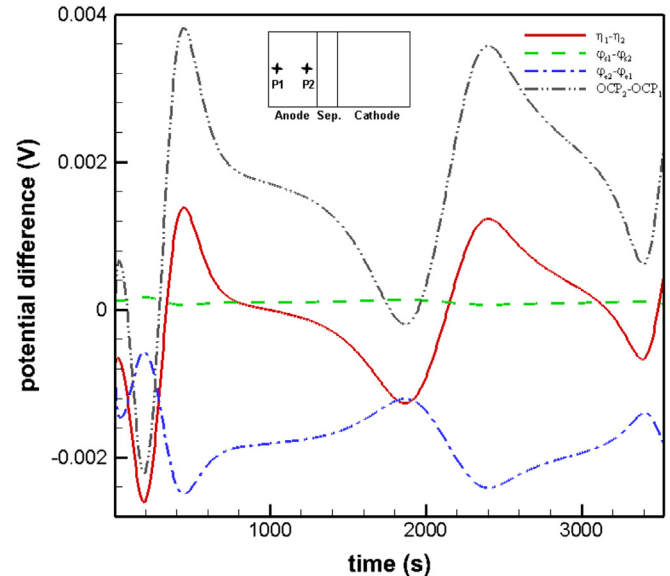


Fig. 12. Temporal evolution of φ_s (and φ_e , OCP, overpotential η) difference between two monitoring points in the anode.

expected. Along the cell thickness direction $C_{s,e}/C_{s,max}$ in the anode shows relatively uniform distribution while in the cathode it decreases with the increase of x .

The spatial and temporal distribution of Li^+ concentration (c_e) in electrolyte during 1C discharge process is depicted in Fig. 14. Upon discharge, a distribution of Li^+ concentration quickly builds up inside the cell, forming a gradient which drives Li^+ species transport along the cell thickness direction from the anode to cathode. Except for the very early period of the discharge process, during which c_e increases in the anode and decreases in the cathode with time, the distribution of c_e shows little change with time.

The heat generations/consumptions in the charge–discharge processes of LiFePO₄/graphite battery include the contact resistance heat, the EC reaction heat, the Joule heat, the ionic migration heat, and the reversible entropy heat. Fig. 15 gives the breakdown of all the heat generations/consumptions during the 1C discharge

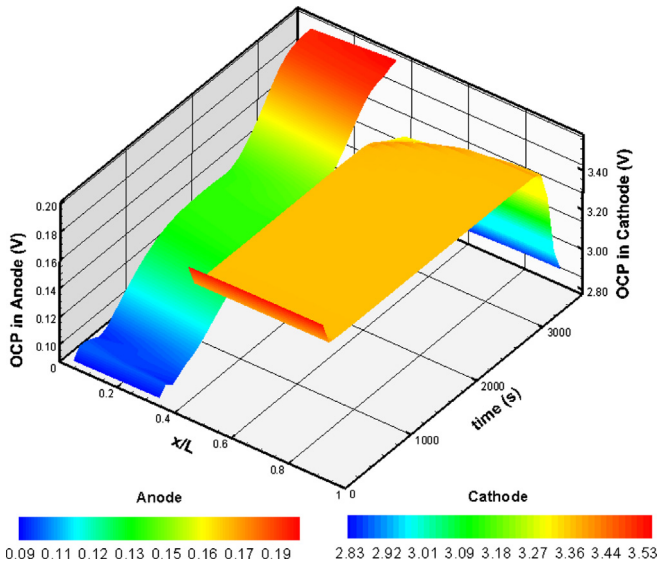


Fig. 11. Spatial and temporal distribution of the OCPs during 1C discharge process.

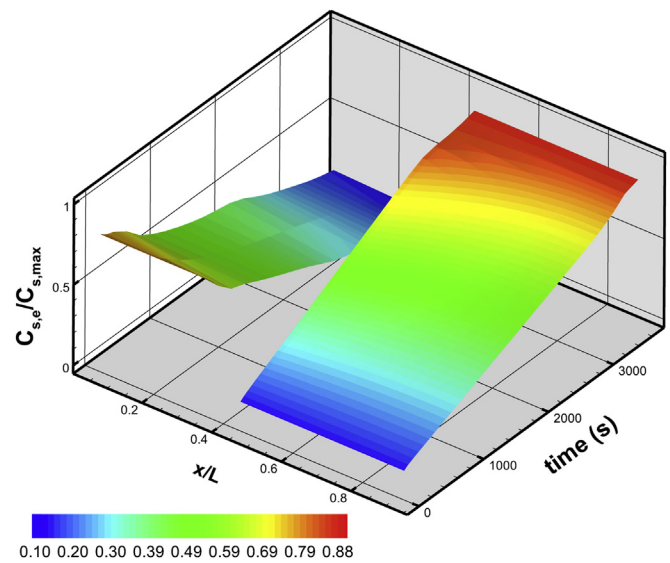


Fig. 13. Spatial and temporal distribution of the $C_{s,e}/C_{s,max}$ during 1C discharge process.

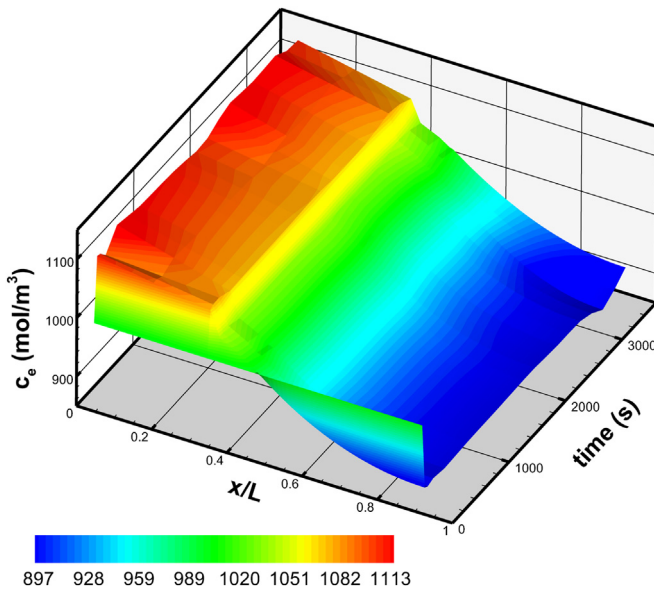


Fig. 14. Spatial and temporal distribution of the Li^+ concentration in electrolyte during 1C discharge process.

process. Note that the heat generations/consumptions are in unit of W, as a volumetric integration of the corresponding source or sink over the whole cell volume has been performed (dimensions of the cell in the other two directions are 0.065 m and 0.1 m, respectively.). Heat generation sources contain the contact resistance heat, the EC reaction heat, and the Joule heat. The ionic migration heat is a heat sink. The reversible entropy heat changes a lot during the discharge process, which is a heat sink in most of the time and becomes a heat source during the late period of the discharge process. The total changing amount of the reversible entropy heat throughout the discharge process is $\sim 0.008 \text{ W}$, comparable to the irreversible EC reaction heat. The contact resistance heat, the EC reaction heat, the Joule heat and the ionic migration heat are almost constant during the discharge process. The irreversible EC reaction heat and contact resistance heat are the two main heat generation sources. About 50–55% of the total heat generation comes from the irreversible EC reaction heat, about 25–30% of the total heat

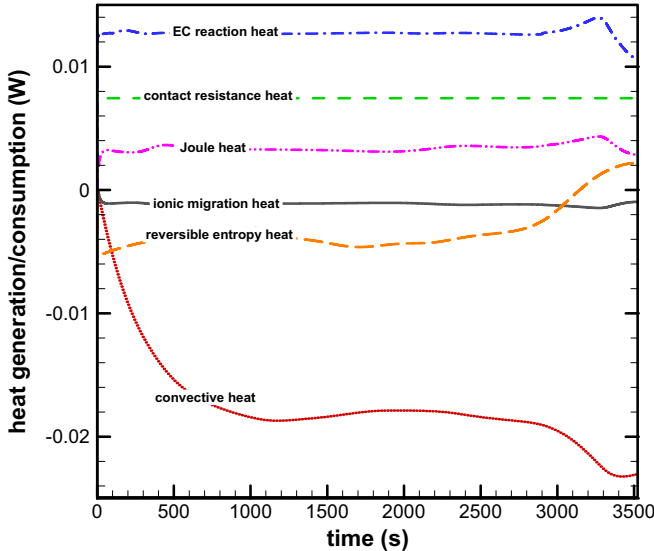


Fig. 15. Thermal analyses of 1C discharge process.

generation is ascribed to the contact resistance heat, and the Joule heat contributes $\sim 15\%$ to the total heat generation. A part of the net heat generation of all the above heat generations/consumptions accumulates in the cell and the other part goes to the ambient by convective heat release.

Fig. 16 shows the spatial profile and temporal evolution of the ionic ohmic heat (W m^{-3}) during the 1C discharge process. At a same time into the discharge process, along the cell thickness direction the ionic ohmic heat increases in the anode and decreases in the cathode with the increase of x ; in the separator it exhibits a minimum value at an interior position, but overall it increases with the increase of x . In the cathode and separator, the ionic ohmic heat increases with time during the very early period of the discharge process, then remains almost unchanged during the middle long period of the discharge process and during the late period (after $\sim 3000 \text{ s}$) of the discharge process the ionic ohmic heat increases first and then decreases. In the anode, the ionic ohmic heat fluctuates with time. At any time instant of the discharge process the maximum ionic ohmic heat is seen to appear always at the cathode/separator interface. The maximum ionic ohmic heat is about 9000 W m^{-3} .

To explain the spatial profile and temporal evolution of the ionic ohmic heat, one may resort to the local ϕ_e gradient, the local ionic current density $i_e (\text{A m}^{-2})$ that is related to the transfer current density, and the ionic conductivity κ that is a function of c_e and takes a maximum value when $c_e = 1.0 \text{ mol L}^{-1}$ (See Fig. 2), as the ionic ohmic heat is calculated as $\kappa^{\text{eff}} \nabla \phi_e \nabla \phi_e$ or $(i_e)^2 / \kappa^{\text{eff}}$. In the separator the ionic current density i_e is location-free and does not change with time, combined with the spatial and temporal distribution of c_e shown in Fig. 14 and the ionic conductivity κ as a function of c_e as depicted in Fig. 2, we find with ease that a minimum ionic ohmic heat appearing at an interior position of the separator is due to the largest ionic conductivity there and the increase of ionic ohmic heat with time during the early period of cell discharge operation is resulted from the decrease of ionic conductivity. In the cathode side at the cathode/separator interface where there exist the largest i_e and relatively small κ , we see the maximum ionic ohmic heat always appears there. In the cathode, stronger EC reaction occurs at positions close to the cathode/separator interface (refer to Fig. 7 for the transfer current density distribution) during the early period of the discharge process, leading to quickly diminishing i_e with the increase of x , which

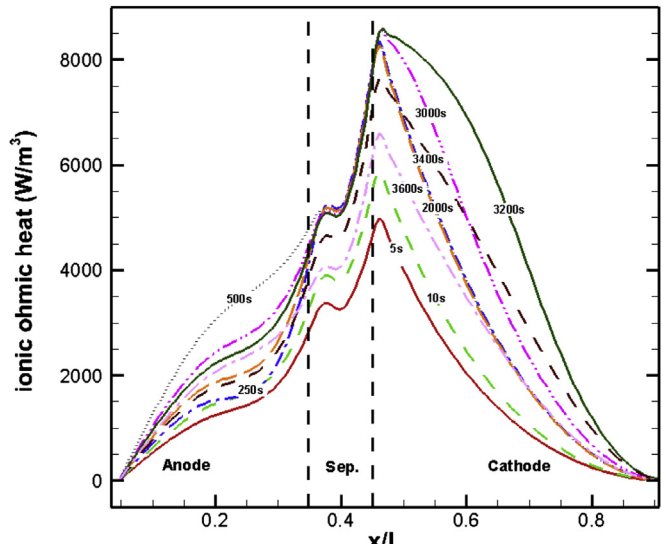


Fig. 16. Spatial profile and temporal evolution of the ionic ohmic heat during 1C discharge process.

dominates over the effect caused by the gradually decreasing κ . Therefore, the ionic ohmic heat is seen to decrease with the increase of x in the cathode. As the c_e (see Fig. 14) and EC reaction rate (see Fig. 7) change little after a short period into the discharge process, the ionic ohmic heat in cathode increases with time during the very early period of the discharge process, then remains almost unchanged in the middle long period of the discharge process. During the late period (after ~ 3000 s) of the discharge process, more portion of the cathode volume has relatively large i_e since the location of maximum EC reaction rate (see Fig. 7) shifts toward the current collector side, leading to increase of the ionic ohmic heat within some time duration (~ 3000 – 3200 s), but afterward it decreases as the discharge process is close to the end. Similarly, we can explain the spatial profile of ionic ohmic heat in the anode. However, the spatial and temporal fluctuations of anode ionic ohmic heat are discerned to be ascribed to the fluctuations of the transfer current density (see Fig. 7).

Fig. 17 shows the spatial profile and temporal evolution of the electronic ohmic heat during 1C discharge process. The electronic ohmic heat is calculated as $\sigma_{\text{eff}}^{\text{eff}} \nabla \varphi_s \nabla \varphi_s$ or $(i_s)^2 / \sigma_{\text{eff}}$, with i_s denoting the electronic current density. Generally, in the cathode the electronic ohmic heat has higher generation rate than in the anode. In the cathode the electronic conductivity σ_s is a constant and the i_s increases with the increase of x . Therefore, we see the electronic ohmic heat increases with the increase of x and takes its maximum rate (~ 90 W m $^{-3}$) at the cathode electrode/current collector interface. As the i_s remains constant at the cathode electrode/current collector interface and zero at separator/electrode interface all-through the cell discharge process, the profiles of electronic ohmic heat in cathode show little change with time. Temporal fluctuations at the electronic ohmic heat are seen in the anode due to the fluctuations of transfer current density (see Fig. 7).

The Joule heat is the summation of the ionic ohmic heat and electronic ohmic heat. Comparing Fig. 16 with Fig. 17, we find that the ionic ohmic heat is about 50 times of the electronic ohmic heat. This is mainly due to the much larger ionic charge transport resistance.

Fig. 18 gives the spatial profile and temporal evolution of the ionic migration heat during the 1C discharge process. The ionic migration heat is negative and thus acts as a heat sink to consume

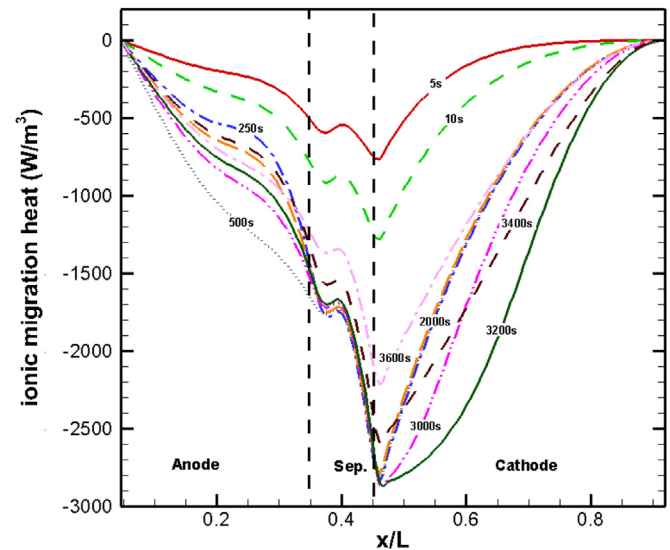


Fig. 18. Spatial profile and temporal evolution of the ionic migration heat during 1C discharge process.

the heat generations. Comparing Fig. 18 with Fig. 16, it is not difficult to find that the ionic migration heat completely resembles the ionic ohmic heat in its spatial profile and temporal evolution except the former is a heat sink and the latter a heat source. The maximum magnitude of the ionic migration heat is ~ 3000 W m $^{-3}$, approximately 1/3 of that of the ionic ohmic heat.

The irreversible heat generation due to EC reaction is directly proportional to the transfer current density and the overpotential, as expressed by Eq. (21). Fig. 19 shows the spatial profile and temporal evolution of the irreversible EC reaction heat during the 1C discharge process. Overall, the EC reaction heat in the cathode is much larger than that in the anode; the maximum EC reaction heat in the cathode is $\sim 35,000$ W m $^{-3}$, about 15 times of that in the anode. The location of the maximum EC reaction heat in the anode changes with time due to the spatial and temporal fluctuations of the transfer current density and overpotential (see Figs. 7 and 8). The maximum EC reaction heat in the cathode is found to appear at the electrode/separator interface during the early period of the

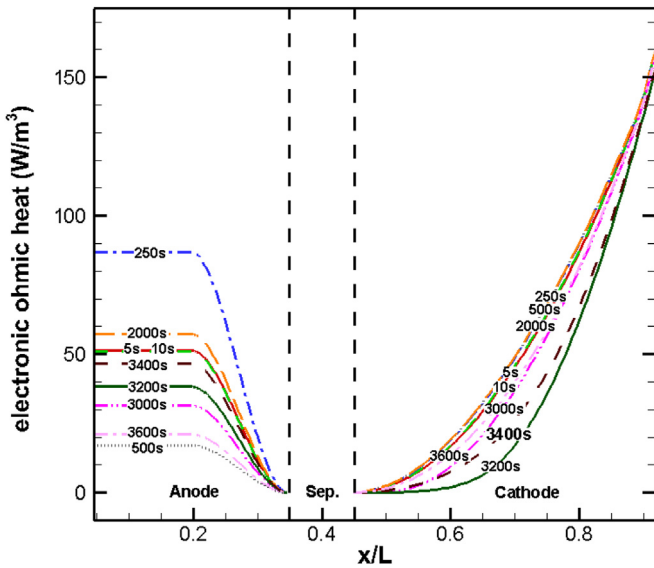


Fig. 17. Spatial profile and temporal evolution of the electronic ohmic heat during 1C discharge process.

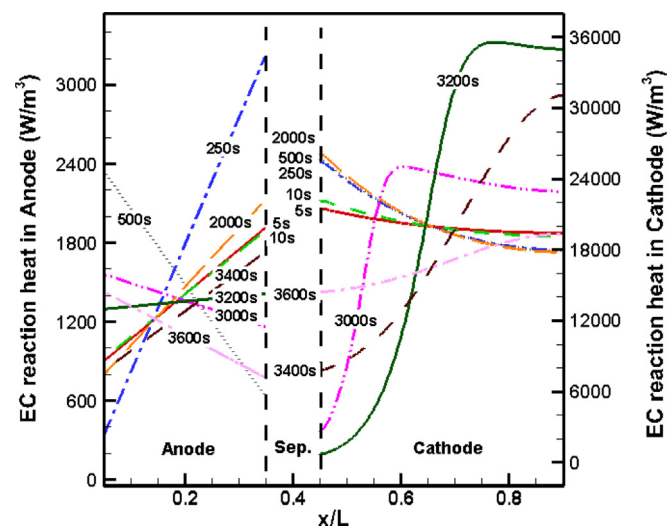


Fig. 19. Spatial profile and temporal evolution of the EC reaction heat during 1C discharge process.

discharge process and at the electrode/current collector interface during the late period (after ~ 3000 s) of the discharge process. The shift of maximum EC reaction heat location in the cathode after about 3000 s into the discharge process is due to the shift of maximum EC reaction intensity and overpotential location (see Figs. 7 and 8).

Fig. 20 gives the spatial profile and temporal evolution of the reversible entropy heat during the 1C discharge. In the anode and cathode both, the reversible entropy heat keeps rising during the discharge process from a negative to positive value. The total changing amount across the discharge process in the anode is $\sim 20,000 \text{ W m}^{-3}$, and in the cathode $\sim 12,000 \text{ W m}^{-3}$, both comparable to the irreversible EC reaction heat. As the reversible entropy heat is directly proportional to the transfer current density as expressed by Eq. (24), due to the spatial and temporal fluctuations of transfer current density in the anode throughout the discharge process and the shift of maximum transfer current density location in the cathode after about 3000 s into the discharge process (see Fig. 7), we see temporal fluctuations of the reversible entropy heat in the anode and the shift of maximum reversible entropy heat location in the cathode after about 3000 s into the discharge process in Fig. 20.

To analyze and compare the temporal evolution of heat generations/consumptions in individual volume of the anode, separator, or cathode, we integrate the corresponding heat generations/consumptions over the anode, separator, and cathode volume, respectively. Results are presented through Figs. 21–24.

It is seen from Fig. 21 that the total Joule heat in the cathode is higher than that in the separator or anode and the total Joule heat in the anode fluctuates with time. All these are in agreement with the observations from Figs. 16 and 17. The total joule heat in the separator or cathode keeps at a constant value of its own during the middle long period of discharge process. During the late period (after ~ 3000 s) of the discharge process, the Joule heat in the cathode increases first and then decreases. The increase is due to the shift of maximum transfer current (see Fig. 7) and the decrease is because the discharge process is approaching the end. However, during the very early period of the discharge process, the Joule heat has relatively lower value, mainly due to relatively smaller deviations of c_e from its optimal value 1.0 mol L^{-1} (See Fig. 14).

Fig. 22 shows the temporal evolution of total ionic migration heat in the anode, separator, and cathode during the 1C discharge process. The total ionic migration heat varies with time in quite

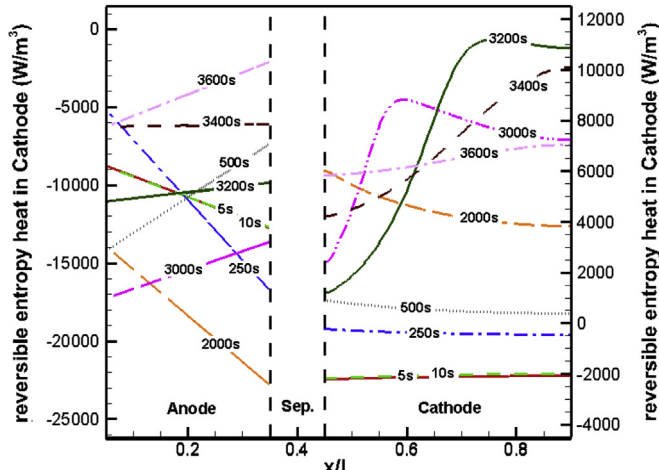


Fig. 20. Spatial profile and temporal evolution of the reversible entropy heat during 1C discharge process.

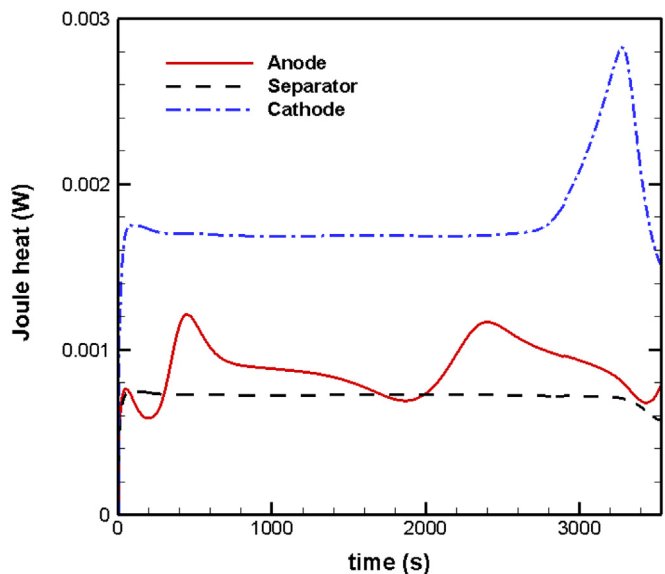


Fig. 21. The total Joule heat in Anode/Separator/Cathode during 1C discharge process.

similar tendency to the total Joule heat except the former is a heat sink and the latter a heat source, in agreement with the observations from Fig. 18.

Fig. 23 shows the temporal evolution of total irreversible EC reaction heat in the anode and cathode during the 1C discharge process. The total irreversible EC reaction heat in the cathode is about 10 times of that in the anode. The total EC reaction heat in the anode or cathode keeps constant during the middle long period of the discharge process. During the late period (after ~ 3000 s) of the discharge process, the EC reaction heat shows a first-increase-then-decrease evolution. The increase of EC reaction heat is mainly due to the shift of maximum transfer current density and the increase of overpotential (see Figs. 7 and 8); the decrease is because the cell discharge process is about to cease.

Fig. 24 shows the temporal evolution of total reversible entropy heat in the anode and cathode during the 1C discharge. The total

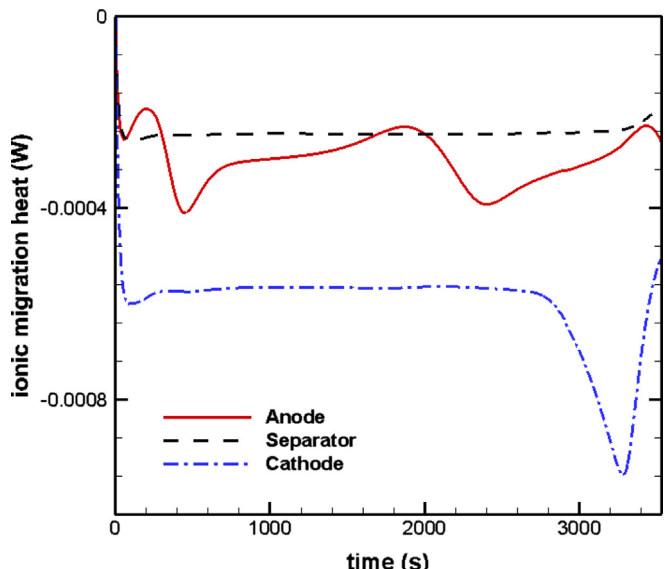


Fig. 22. The total ionic migration heat in Anode/Separator/Cathode during 1C discharge process.

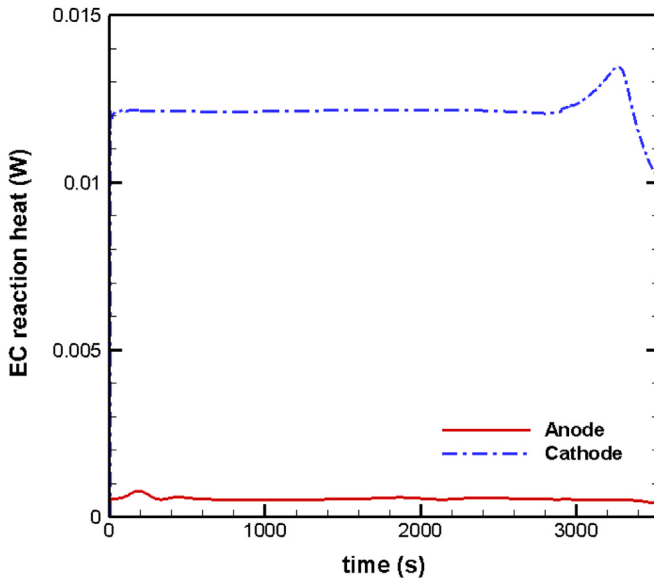


Fig. 23. The total EC reaction heat in Anode/Cathode during 1C discharge process.

reversible entropy heat in the cathode increases monotonically with time all-through the discharge process except during the very late period (after ~ 3000 s) of the discharge process; in the anode it decreases during a middle period and increases in the late period of the discharge process. The total reversible entropy heat can either act as a heat sink or a heat source.

Figs. 25 and 26 summarize the breakdown of all the heat generations/consumptions during the 3C and 5C discharge processes, respectively. As the contact resistance heat and Joule heat are both directly proportional to the square of discharge current density (see Eqs. (22) and (27)), they take more proportion of the total heat generation if the C-rate is higher. For the 3C discharge process, about $\sim 40\%$ of the total heat generation comes from the irreversible EC reaction heat, about $\sim 42\%$ of the total heat generation is ascribed to the contact resistance heat, and the Joule heat contributes $\sim 16\%$ to the total heat generation. For the 5C discharge

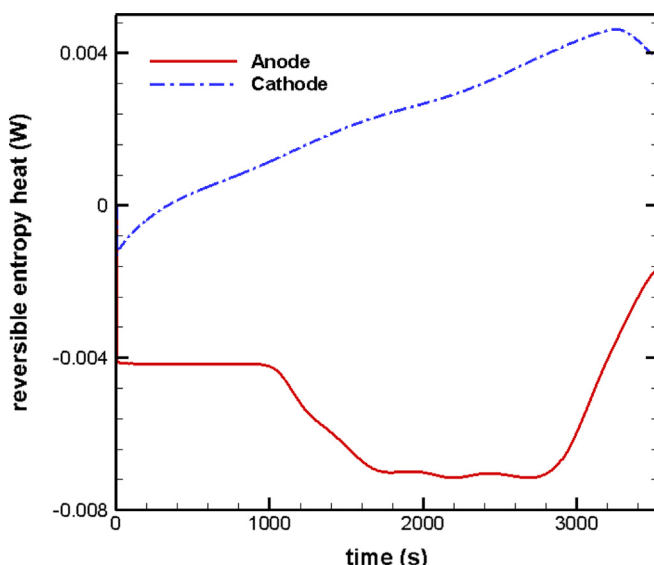


Fig. 24. The total reversible entropy heat in Anode/Cathode during 1C discharge process.

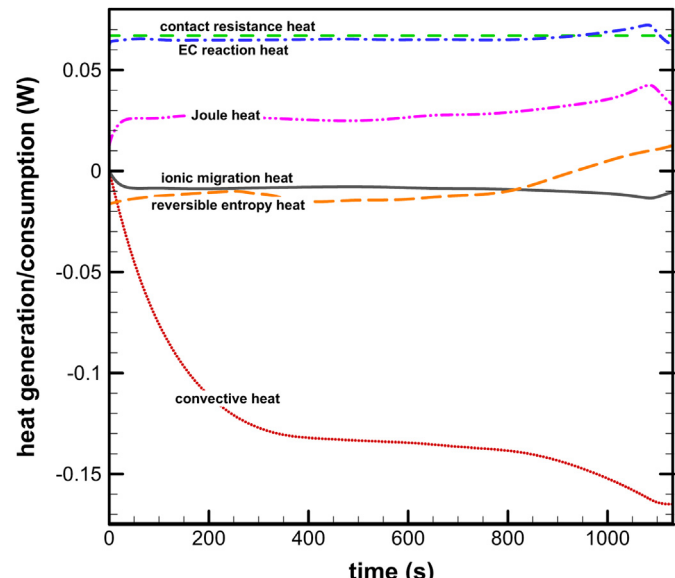


Fig. 25. Thermal analyses of 3C discharge process.

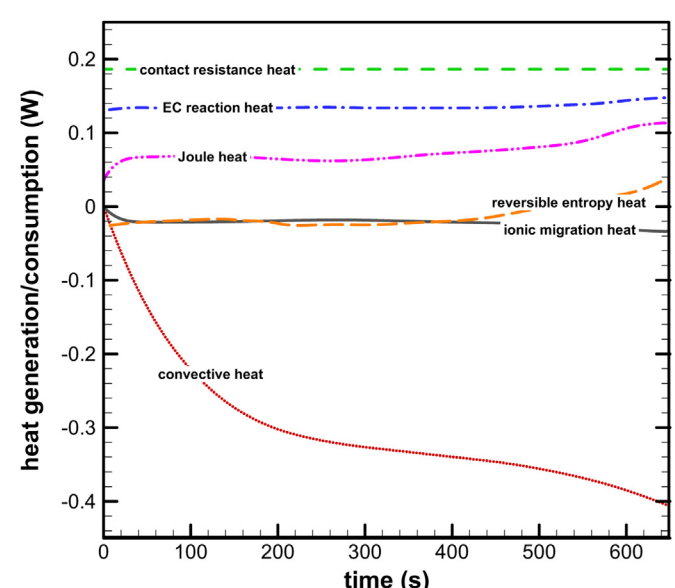


Fig. 26. Thermal analyses of 5C discharge process.

process, the total heat generation consists of $\sim 35\%$ EC reaction heat, $\sim 50\%$ contact resistance heat, and $\sim 15\%$ Joule heat.

The reversible entropy heat has important effect on the temperature evolution of the cell during discharge processes. The changing magnitude of the reversible entropy heat all-through the 3C discharge process is about 0.03 W, and 0.05 W for the 5C discharge process, both comparable to the corresponding irreversible EC reaction heat. However, due to the contact resistance heat and Joule heat take more and more portion of the total heat generation with the increase of C-rate, the effect of reversible entropy heat is diminishing.

5. Conclusions

Analyzing thermal behaviors is very important to the design and operation and the thermal management of Li-ion batteries. An

electrochemical–thermal (ECT) coupling model, which accounts for the multidisciplinary coupling effect and solves the inter-coupled charge (ion in the electrolyte phase and electron in the solid phase), species (Li^+ in the electrolyte and lithium in the electrode active materials), and energy conservation equations has been developed for LiFePO_4 /graphite batteries. During modeling, a lumped-treatment to the contact resistance at the current collector/electrode interfaces and the impedance due to the SEI layers has been implemented by defining a total contact resistance based on the side surface area of the electrode plate. Experimental validation to the ECT model was first performed, during which the spatial and temporal dependence of electric contact resistance were disregarded and a same constant contact resistance for discharge processes of different C-rates was specified. The experimentally validated ECT model was then applied to analyze the thermal behaviors of a LiFePO_4 /graphite battery at various discharge C-rates. The calculated results gave insightful detailed information about thermal behaviors and performance of the battery. For the specific cell considered, breakdown of various heat generations/consumptions including the Joule heat, reversible entropy heat, contact resistance heat, irreversible EC reaction heat, ionic migration heat indicates that the EC reaction heat and contact resistance heat are the two main heat generation sources during discharge processes; the ionic migration heat is always a heat sink, the magnitude of which is about 1/3 of the ionic ohmic heat. Some general hints obtained for the thermal design of a battery in practice include such as, the contact resistance heat may take more proportion of the total heat generation during discharge processes of higher C-rate as it is directly proportional to the squared current load; the reversible entropy heat may result in large temperature rise during the late period of discharge processes as it changes from a heat sink to a heat source and the changing magnitude is comparable to the EC reaction heat.

Acknowledgments

This study was financially supported by Amperex Technology Limited (ATL-Dongguan), the CAS Key Laboratory of Renewable Energy Foundation (y307j91001), and the CAS “100 Talents” Program (FJ). The authors also acknowledge the significant

contribution to the scientific quality of this work made by the anonymous reviewers.

References

- [1] A.K. Padhi, K.S. Nanjundaswamy, J.B. Goodenough, *J. Electrochem. Soc.* 144 (1997) 1188–1194.
- [2] C.R. Pals, J. Newman, *J. Electrochem. Soc.* 142 (1995) 3274–3281.
- [3] C.R. Pals, J. Newman, *J. Electrochem. Soc.* 142 (1995) 3282–3288.
- [4] K. Kumaresan, G. Sikha, R.E. White, *J. Electrochem. Soc.* 155 (2008) A164–A171.
- [5] W.B. Gu, C.Y. Wang, *J. Electrochem. Soc.* 147 (2000) 2910–2922.
- [6] M. Doyle, T.F. Fuller, J. Newman, *J. Electrochem. Soc.* 140 (1993) 1526–1533.
- [7] T.F. Fuller, M. Doyle, J. Newman, *J. Electrochem. Soc.* 141 (1994) 1–10.
- [8] V. Srinivasan, C.Y. Wang, *J. Electrochem. Soc.* 150 (2003) A98–A106.
- [9] X.W. Zhang, *Electrochim. Acta* 56 (2011) 1246–1255.
- [10] Y.H. Ye, Y.X. Shi, N.S. Cai, J.J. Lee, X.M. He, *J. Power Sources* 199 (2012) 227–238.
- [11] C.Y. Wang, W.B. Gu, *J. Electrochem. Soc.* 145 (1998) 3407–3417.
- [12] V. Srinivasan, J. Newman, *J. Electrochem. Soc.* 151 (2004) A1517–A1529.
- [13] Q. Zhang, R.E. White, *J. Electrochem. Soc.* 154 (2007) A587–A596.
- [14] C. Wang, U.S. Kasavajjula, P.E. Arce, *J. Phys. Chem. C* 111 (2007) 16656–16663.
- [15] U.S. Kasavajjula, C. Wang, P.E. Arce, *J. Electrochem. Soc.* 155 (2008) A866–A874.
- [16] S. Dargaville, T.W. Farrell, *J. Electrochem. Soc.* 157 (2010) A830–A840.
- [17] L. Laffont, C. Delacourt, P. Gibot, M.Y. Wu, P. Kooyman, C. Masquelier, J.M. Tarascon, *Chem. Mater.* 18 (2006) 5520–5529.
- [18] G. Chen, X. Song, T.J. Richardson, *Electrochim. Solid State Lett.* 9 (2006) A295–A298.
- [19] A.S. Andersson, J.O. Thomas, *J. Power Sources* 97 (2001) 498–502.
- [20] B.C. Han, A. Van der Ven, D. Morgan, G. Ceder, *Electrochim. Acta* 49 (2004) 4691–4699.
- [21] G.K. Singh, G. Ceder, M.Z. Bazant, *Electrochim. Acta* 53 (2008) 7599–7613.
- [22] D. Burch, G.K. Singh, G. Ceder, M.Z. Bazant, *Solid State Phenom.* 139 (2008) 95–100.
- [23] D. Burch, M.Z. Bazant, *Nano Lett.* 9 (2009) 3795–3800.
- [24] M. Safari, C. Delacourt, *J. Electrochem. Soc.* 158 (2011) A63–A73.
- [25] V. Srinivasan, J. Newman, *Electrochim. Solid State Lett.* 9 (2006) A110–A114.
- [26] I.V. Thorat, Ph.D Thesis, Brigham Young University, 2009.
- [27] M. Farkhondeh, C. Delacourt, *J. Electrochem. Soc.* 159 (2012) A177–A192.
- [28] M. Park, X.C. Zhang, M. Chung, G.B. Less, A.M. Sastry, *J. Power Sources* 195 (2010) 7904–7929.
- [29] W.F. Fang, O.J. Kwon, C.Y. Wang, *Int. J. Energy Res.* 34 (2010) 107–115.
- [30] L.O. Vloen, J.N. Reimers, *J. Electrochem. Soc.* 152 (2005) A882–A891.
- [31] M. Guo, G. Sikha, R.E. White, *J. Electrochem. Soc.* 158 (2011) A122–A132.
- [32] R.E. Gerber, MS Dissertation, The University of Texas at Austin, 2009.
- [33] G.G. Fang, L. Bo, C. Bo, Z.S. Qiong, X. Peng, C.B. Gang, *J. Power Sources* 195 (2010) 2393–2398.
- [34] K. Somasundaram, E. Birgersson, A.S. Mujumdar, *J. Power Sources* 203 (2012) 84–96.